

Synthesis and Physical Properties of Phase-Engineered Transition Metal Dichalcogenide Monolayer Heterostructures

Carl H. Naylor,¹ William M. Parkin,¹ Zhaoli Gao,¹ Joel Berry,² Songsong Zhou,² Qicheng Zhang,¹ John Brandon McClimon,² Liang Z. Tan,³ Christopher E. Kehayias,¹ Meng-Qiang Zhao,¹ Ram S. Gona,¹ Robert W. Carpick,^{2,4} Andrew M. Rappe,³ David J. Srolovitz,^{2,4} Marija Drndic,¹ Alan T. Charlie Johnson^{1}*

¹Department of Physics and Astronomy, University of Pennsylvania,

²Department of Materials Science and Engineering, University of Pennsylvania,

³Department of Chemistry, University of Pennsylvania,

⁴Department of Mechanical Engineering and Applied Mechanics, University of Pennsylvania,

Philadelphia, Pennsylvania 19104, United States

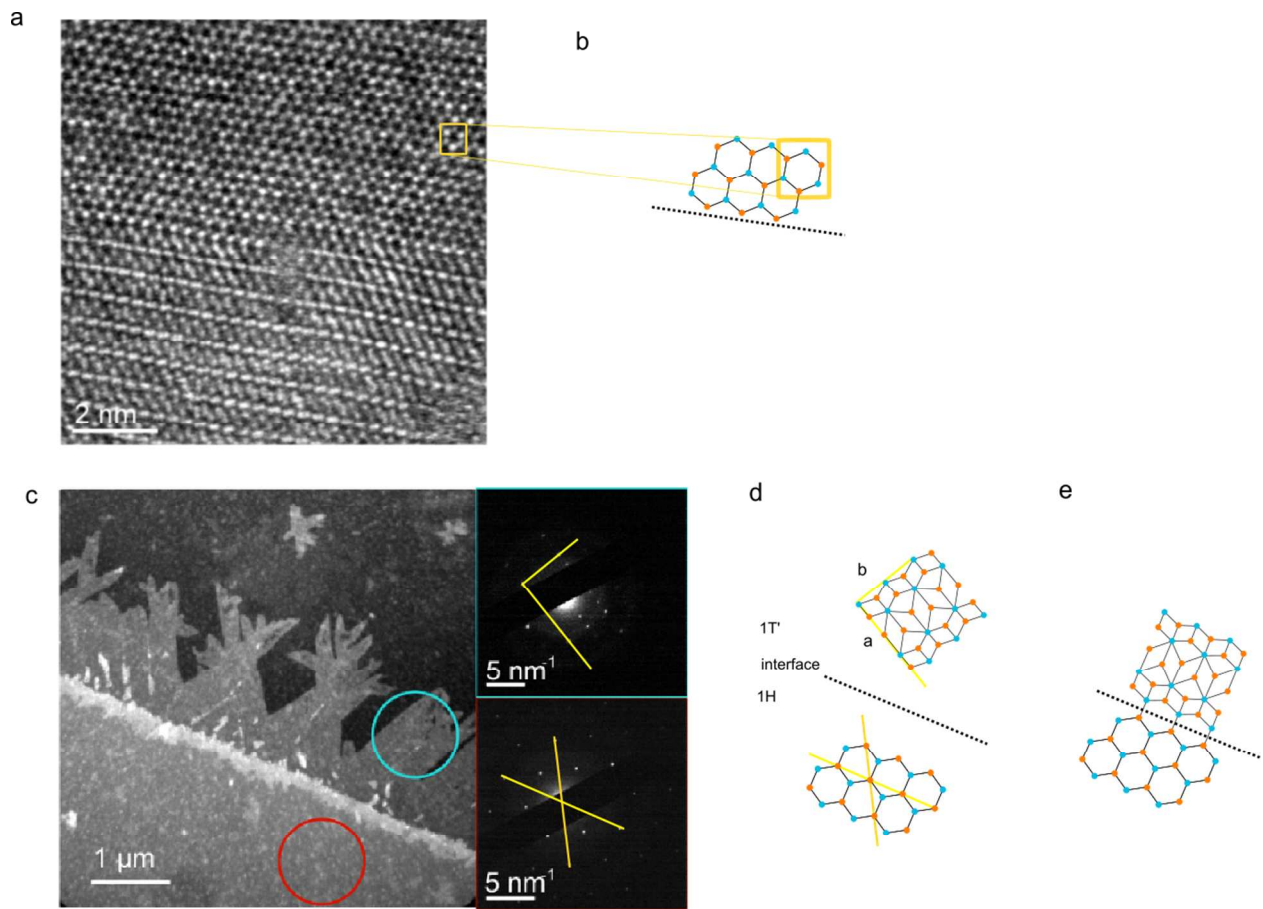


Figure S1. SAED and ACSTEM determination of lattice orientation. a) ACSTEM image from Figure 3d. b) The orientation of the chalcogen atoms around the hexagonal lattice (in yellow box, chalcogen sites have two Te atoms) determines that the edge of the 1H region is chalcogen zigzag. c) Dark-field TEM image and SAED images from Figure 3a. The direction of the orthogonal lattice vectors in the 1T' region are easily read from the SAED pattern. The angle between the interface and the short real-space lattice vector is measured to be either 60deg or 120deg for 1T' regions far from the interface. In the 1H region, the real-space lattice vectors are parallel to the (2 -1 -1 0) reflections. The interface is parallel to a 1H lattice vector, so the 1H region has zigzag edges. d) Expected lattice orientation at the interface as determined by SAED of 1T' regions far from the interface. e) Actual atom arrangement at the interface as determined by ACSTEM.

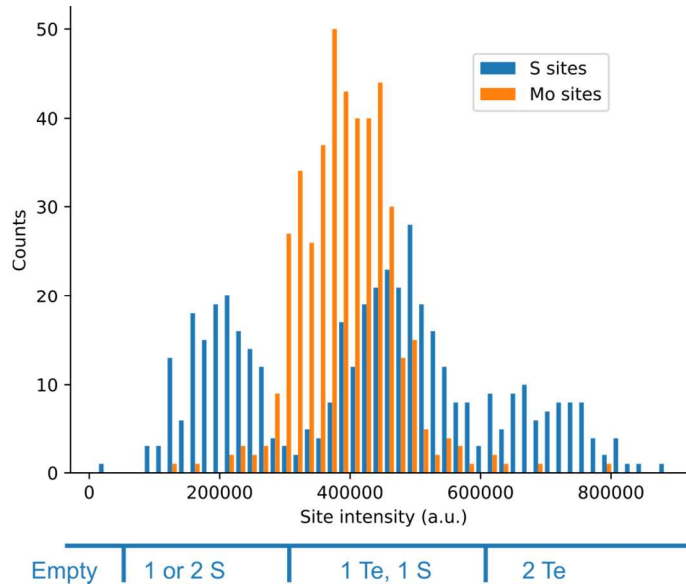


Figure S2. Intensity of S and Mo sites in Figure 3e. HAADF is mass contrast, so the sites were labelled based on the fact that the intensities should be in order of empty < 1 S or 2 S < Mo < 1 Te and 1 S < 2 Te. Site positions were identified by hand, and site intensity plotted is the mean image intensity of the pixels within the site. Narrower histograms and better site identification could be achieved with cleaner samples and a reduction in hydrocarbon contamination.

CHARACTERIZATION OF 1H/1T' HETEROSTRUCTURES

A quasi-2D buckling analysis indicates that the width of the buckled region, $\ell_0 \approx 500$ nm, is much too large to be caused by interfacial misfit strain alone. Compressive stress localized at the edge of a free 2D sheet induces 1D wrinkles oriented perpendicular to the edge that decay into the sheet over a length scale $\ell_0 \approx 0.23\lambda$ [1]. For $\lambda \approx 25$ nm, the predicted value $\ell_0 \approx 6$ nm is much less than the observed value $\ell_0 \approx 500$ nm. The wrinkling morphology is also generally 2D/worm-like away from the interface, which is consistent with biaxial compression induced by Te substitution as opposed to uniaxial

compression induced by 1D interfacial misfit.

Modulations of Te composition in the 1H phase may also result from thermodynamically-driven phase separation into Te-rich and Te-poor phases upon quenching below $T \lesssim 230^\circ\text{C}$. Without knowledge of S and Te transport rates in this temperature range, it is unclear whether such phase separation is kinetically feasible. Our TERS and DFPT results are consistent with the onset of this phase separation process, followed quickly by stagnation at nanoscale domain sizes due to kinetic limitations. ACSTEM observations of small 1H phase subdomains on the T' side of the interface are also consistent with the formation of a phase separated Te-rich 1H phase near the initial interface, followed by incomplete transformation of this region to 1T'.

FIRST-PRINCIPLES CALCULATIONS OF 1T'-MoTe₂ EDGE ENERGIES

First-principles density functional theory (DFT) calculations of 1T'-MoTe₂ edge energies were performed using the Vienna Ab-initio Simulation Package (VASP) using a plane-wave basis set [2, 3] and the projector augmented wave method [4]. The generalized gradient approximation [5] with the Perdew-Burke-Ernzerhof functional [6] was used to treat exchange correlation effects. All edge structures were fully relaxed until the total force on each atom was less than 0.01 eV/Å. A vacuum layer of minimum thickness of 20 Å perpendicular to the monolayer was employed to minimize interactions between each monolayer and its periodic images. The kinetic energy cutoff was set to 420 eV, and the Γ -centered k-point grid up to 12×1×1 was used for Brillouin zone integration. We employed the same approach used earlier to determine the 1T'-MoS₂ edge energies [7].

Zigzag (*b* axis) edges in the 1T' unit cell may occur in six different configurations, depending on the edge termination (see Figure S3). These edges may be non-stoichiometric (i.e., Mo- or Te-rich), and thus their energy is a function of the relative chemical potential of the constituents. Our results (Figure

S3) show that the stable zigzag edge energy γ_z (that with lowest energy among all six possible configurations at a given chemical potential) is 200 meV/Å or less (depending on the chemical potential). The armchair (a axis) edge has only one configuration, which is stoichiometric, and thus its energy is independent of chemical potential; i.e. $\gamma_A \approx 270$ meV/Å (green line in Figure S3). This is significantly higher than γ_z .

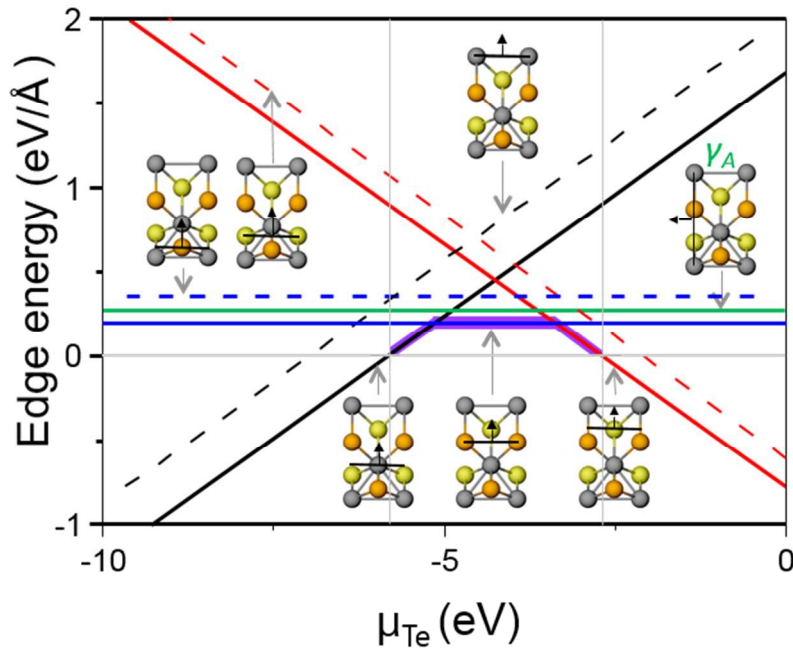


Figure S3. Energies of the seven 1T' MoTe₂ edges as a function of chemical potential of Te. Dashed lines denote zigzag edges that are never the lowest energy of the six zigzag configurations. Vertical gray lines enclose the stable range of chemical potentials for zigzag edges, and the horizontal gray line indicates zero energy. The lines highlighted in purple indicate the three lowest energy zigzag boundaries and their energies over the stable range of μ_{Te} . Configurations of each edge are denoted by black lines and arrows. Black lines mark the location of the edges (where the unit cell is cut to create the edges), arrows are perpendicular to the edge and point from the 1T' phase toward vacuum.

EQUILIBRIUM 1T'-MoTe₂ ISLAND SHAPES

The edge energies computed above and the rectangular symmetry of the 1T' unit cell are sufficient to determine that the equilibrium 1T' island shape is elongated along the b or zigzag axis of the unit cell. The precise shape and degree of elongation depend on the values of γ at all edge orientations ϕ (measured relative to the armchair orientation) for a given chemical potential. Since we do not know these dependencies, we will assume a simple functional form of $\gamma(\phi)$ that allows us to generate estimates of 1T' island axial ratios (AR) from a standard equilibrium Wulff construction. The 1T' lattice exhibits a pair of 2-fold rotation axes. We expect in general that the zigzag and armchair orientations will correspond to local minima of $\gamma(\phi)$. Since the experimental observations show faceted edges, we further assume that these minima correspond to cusps. The following trial functional form of $\gamma(\phi)$ ensures cusps, the appropriate symmetry, and has two parameters that are in principle functions of γ_A and γ_Z : $\gamma(\phi) \simeq \bar{\gamma} [1 + B \cos(\phi + C)]$ for $0 \leq \phi \leq \pi/2$. $\bar{\gamma}$, B , and C are constants; we set $C = 0.16$ (this gives a shallow cusp at $\phi = 0$ and a deeper cusp at $\phi = \pi/2$) and vary $\bar{\gamma}$ and B such that $\gamma(\pi/2) = \gamma_Z$ decreases while $\gamma(0) = \gamma_A$ remains fixed (see Figure S4). This allows approximate island shapes at various ratios of γ_Z/γ_A to be determined. By comparing the AR of these shapes with experimental observations, the value of γ_Z and the chemical potential μ_{Te} during growth are estimated.

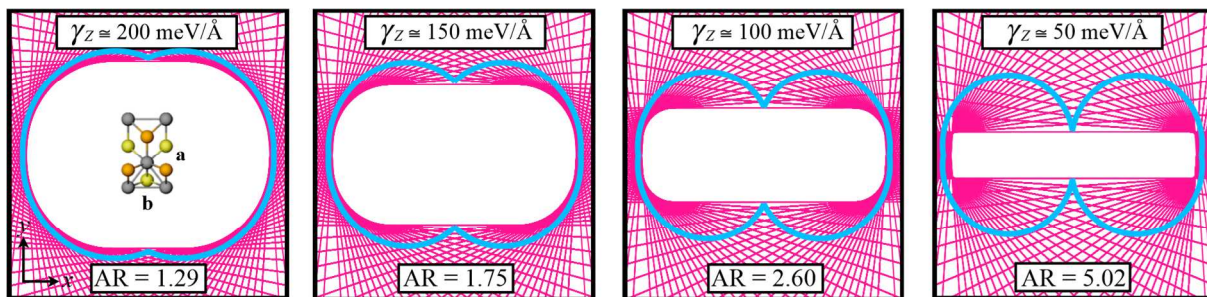


Figure S4. Computed equilibrium 1T' island shapes (the inner contour traced by the pink lines) for increasingly anisotropic and cusped edge energy functions of the form $\gamma(\phi) \simeq \bar{\gamma}[1 + B \cos(\phi + C)]$ (blue lines). The value of γ_Z consistent with each shape is noted (γ_Z is taken as fixed at 270 meV/Å). The cusps

in $\gamma(\phi)$ at $\phi = 0$ and π are too shallow to be clearly discernible in some cases.

The equilibrium island shapes corresponding to this function are either rectangular or rectangular with rounded corners, as shown in Figure S4 for several possible ratios of γ_z/γ_A (depending on the chemical potential). This is consistent with the shapes reported in experimental studies [8–10]. The present results suggest that the 1T' islands will have aspect ratios AR in the range $1.29 \leq AR \leq \infty$. The average aspect ratio extracted from the experimental images in Refs. [8, 9] is $AR \simeq 4.5 - 6$, which falls within this range and is consistent with $\gamma_z \simeq 40 - 60$ meV/Å. The corresponding chemical potential during growth is either $\mu_{Te} \simeq -3$ eV or -5.5 eV. The flakes grown in Ref. [10] are somewhat more elongated; we find $AR \simeq 7$ on average. This value is consistent with $\gamma_z \simeq 20 - 30$ meV/Å and $\mu_{Te} \simeq -2.8$ eV or -5.7 eV. Our findings also indicate that the dual 2-fold symmetry of 1T' crystals combined with the dependence of edge energies on chemical potential can enable direct growth of extremely long 1T'-MoTe₂ nanoribbons at suitably controlled values of μ_{Te} ($AR \rightarrow \infty$ as $\gamma_z \rightarrow 0$).

The rectangular nature of these islands differs from the triangular or hexagonal flakes seen in materials with a hexagonal structure (e.g., graphene, BN, and 1H-TMDs) because of the crystal symmetry of the 1T' unit cell. Like these hexagonal crystals, the observed 1T' island shapes can be understood as a consequence of edge energy anisotropy and the symmetry of the unit cell rather than, e.g., strong kinetic effects. The needle-like 1T' morphologies observed in the MoS₂/MoTe₂ heterostructures reported in this work are qualitatively consistent with this finding, though the additional effect of misfit strain between the 1H and 1T' phases also plays a role, as demonstrated in the following section.

PHASE FIELD SIMULATIONS OF HETEROSTRUCTURE GROWTH

The continuum phase field simulations presented in the main text employ a modified version of

a phase field microelasticity (PFM) model constructed to describe displacive $1H \rightarrow 1T'$ transformations in TMD monolayers [11]. This formulation provides numerical solutions of the piecewise linear elasticity equations for coherent, elastically misfitting bodies within a matrix or parent phase. Domains of the different phases are described in terms of structural order parameter fields $\eta_p(\vec{r})$ that evolve to minimize the total energy of the system, which is composed of bulk chemical, interfacial, and elastic contributions. The relevant order parameter fields are those that distinguish the different $1T'$ orientations (variants) and the H structure. The free energy functional F_{tot} for the structurally inhomogeneous monolayer is

$$F_{\text{tot}} = \int_A (f_{\text{chem}} + f_{\text{elas}}) dA \quad (1)$$

where

$$f_{\text{chem}} = \sum_p \left(\frac{a}{2} \eta_p^2 - \frac{b}{4} \eta_p^4 \right) + \frac{c}{6} \left(\sum_p \eta_p^2 \right)^3 + \sum_p \left(\frac{P(\vec{r})}{2} \eta_p^2 + \frac{d}{3} H(\eta_p) \eta_p^3 + \frac{1}{2} |\beta_p(\Phi) \nabla \eta_p|^2 \right) \quad (2)$$

and

$$f_{\text{elas}} = \frac{h}{2} \lambda_{ijkl} \epsilon_{ij} \epsilon_{kl} + h \sum_p \left[\frac{1}{2} \lambda_{ijkl} \epsilon_{ij}^0(p) \epsilon_{kl}^0(p) \eta_p^4 - \lambda_{ijkl} \epsilon_{ij}(p) \epsilon_{kl}^0(p) \eta_p^2 \right] \quad (3)$$

f_{chem} is the stress-free energy density of the monolayer, and f_{elas} is the elastic energy density which contains all self and elastic interaction energy densities associated with the arbitrary configuration of structural domains within the monolayer. Summations are taken over the $1T'$ variant order parameter fields denoted by index p , and strains are measured with respect to the stress-free $1H$ parent phase. The adjustable constants a , b , and c set the magnitude of the chemical driving force for $1T'$ growth. $P(\vec{r})$ and d modulate the energy landscape as described below, and $H(\eta_p)$ is the Heaviside step function. The parameter $\beta_p(\Phi)$ is proportional to the interfacial energy and is taken here to be either independent of

interface inclination angle ϕ or to have the anisotropy determined from the first-principles calculations above.

The first three terms in f_{chem} compose the simplest polynomial consistent with the symmetries of the $1\text{H} \rightarrow 1\text{T}'$ transformation, and is the same form previously incorporated into a 2D PFM model of hexagonal to orthorhombic transformations [12–14]. Of the twelve total $1\text{T}'$ variants (three orientations, four subvariants at each orientation, see Figure S5b), this functional describes six (two subvariants at each orientation) in terms of three order parameter fields. Symmetric energy minima at $\eta_p = -1$ and 1 represent p^- and p^+ domains, respectively (see Figure S5b), while regions where all $\eta_p = 0$ correspond to H domains. Since we are more interested in distinguishing between the three $1\text{T}'$ orientations than between the subvariants at each orientation, for simplicity we have added a term proportional to η_p^3 that suppresses the $\eta_p = 1$ minima. In this way, all four subvariants at each $1\text{T}'$ orientation p are combined into the single energy minimum at $\eta_p = -1$ (Figure S5c).

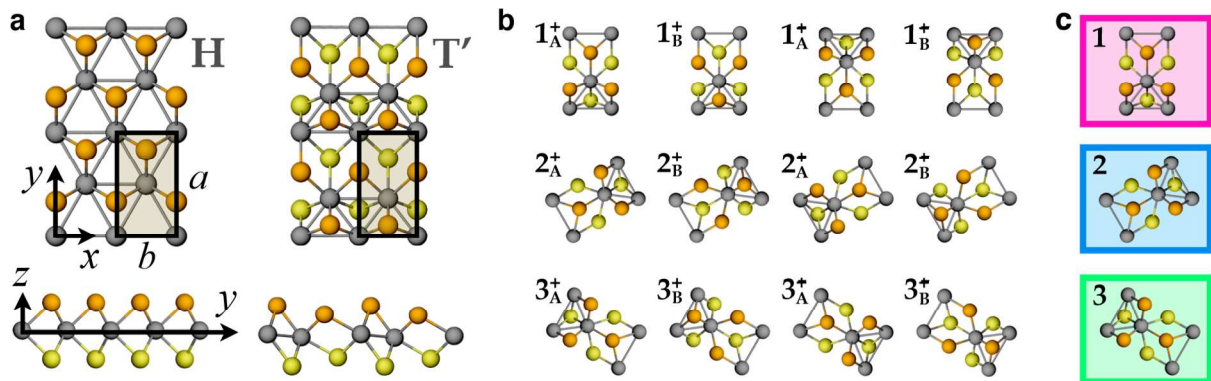


Figure S5. 1H and $1\text{T}'$ crystal structures and orientational variants. **a.** Metal and upper/lower chalcogen atoms are shown in gray and orange/yellow, respectively. **b.** The 12 $1\text{T}'$ orientational variants designated p_{α}^{\pm} , where $p \in \{1,2,3\}$, superscripts (\pm), and subscripts $\alpha \in \{A,B\}$ distinguish between orientation, direction of dimerization, and direction of x - y mirror asymmetry, respectively. **c.** Simplification to three variants used in the present work. Colored boxes indicate the scheme employed

for simulation visualization.

In f_{elas} , h is the monolayer thickness, λ_{ijkl} is the elastic stiffness tensor, $\epsilon_{ij}^0(p) = \mathbf{R}[\theta_p] \epsilon_{ij}^0 \mathbf{R}^T[\theta_p]$ is the transformation strain tensor of variant p , and $\epsilon_{ij}(\vec{r}) = \bar{\epsilon}_{ij} + \frac{1}{2}(u_{i,j} + u_{j,i})$ is the elastic strain tensor ($i,j,k,l = x,y$). $\mathbf{R}[\theta_p]$ is the 2D rotation matrix, $\epsilon_{xx}^0 = (b_{1T'} - b_{1H})/b_{1H}$; $\epsilon_{yy}^0 = (a_{1T'} - a_{1H})/a_{1H}$; $\epsilon_{xy}^0 = 0$; $\theta_1 = 0$; $\theta_2 = 2\pi/3$ and $\theta_3 = -2\pi/3$. u_i are in-plane displacements and $\bar{\epsilon}_{ij}$ is the externally imposed, applied macroscopic strain. The equations of thermomechanical equilibrium for in-plane displacements $u_i(\vec{r})$ and order parameters $\eta_p(\vec{r})$ are

$$\lambda_{ijkl} k_j k_k \hat{u}_l(\vec{k}) = -i \sum_{p=1}^3 \sigma_{ij}^0(p) k_j \widehat{\eta}_p^2(\vec{k}) \quad (4)$$

and

$$2\lambda_{ijkl} \epsilon_{kl}^0(p) \eta_p [\epsilon_{ij}^0(p) \eta_p^2 - \bar{\epsilon}_{ij} - 1/2 (u_{i,j} + u_{j,i})] = 0 \quad (5)$$

respectively, where k is wavenumber, $\hat{u}_i(\vec{k})$ is the Fourier transform of $u_i(\vec{r})$, $\sigma_{ij}^0(p) = \lambda_{ijkl} \epsilon_{kl}^0(p)$ are the elements of the transformation stress tensor, and $\widehat{\eta}_p^2(\vec{k})$ is the Fourier transform of $\eta_p^2(\vec{r})$.

We explicitly solve for u_i and η_p using a combined analytical/numerical approach. Exact analytic solutions for u_x and u_y are first obtained by solving Eq. (4) as

$$\hat{u}_i(\vec{k}) = -i \sum_p G_{ij}(\vec{k}) \sigma_{jk}^0(p) k_k \widehat{\eta}_p^2(\vec{k}) \quad (6)$$

where $G_{ij}(\vec{k}) = \Omega_{ij}(\vec{n})/k^2$, $\Omega_{ij}^{-1} = \lambda_{ijkl} n_k n_l$, and $\vec{n} = \vec{k}/|k|$. For simplicity, we assume that the elastic constants of the material are isotropic and that plane stress conditions apply such that $\lambda_{ijkl} = \mu[\delta_{ik}\delta_{jl} + \delta_{il}\delta_{jk} + 2\nu/(1-\nu)\delta_{ij}\delta_{kl}]$ and the elastic Green's function is given by $G_{ij}(\vec{k}) = \delta_{ij}/\mu k^2 - (1 + \nu)k_i k_j / 2\mu k^4$, where \vec{k} is wave vector and $k^2 = k_x^2 + k_y^2$. μ and ν are the shear modulus and Poisson's ratio of the monolayer, respectively.

All η_p are then iterated toward thermomechanical equilibrium by identical small increments of time t using equations of the form

$$\eta_{p,t} = -M_p \frac{\delta F_{\text{tot}}}{\delta \eta_p} + v_p \quad (7)$$

or

$$\eta_{p,t} = M_p \nabla^2 \frac{\delta F_{\text{tot}}}{\delta \eta_p} + \tilde{v}_p \quad (8)$$

where M_p are mobility constants. Equation (7) phenomenologically describes evolution toward thermodynamic equilibrium in the absence of a conservation law for the area of 1T' phase in the plane of the monolayer. This equation is most appropriate when the supply of constituent atoms is not the rate limiting factor in 1T' growth. v_p is a Gaussian noise variable with $\langle v_p \rangle = 0$ and $\langle v_p(\vec{r}, t) v_p(\vec{r}', t') \rangle = -2k_B T \delta(\vec{r} - \vec{r}') \delta(t - t')$. Equation (8) is a generalized diffusion equation that describes evolution toward thermodynamic equilibrium when the area of 1T' phase in the plane of the monolayer is conservatively controlled by an external source. This form is appropriate when the supply of constituent atoms and their migration above or on the surface of the monolayer limit 1T' growth. \tilde{v}_p is a Gaussian noise variable with $\langle \tilde{v}_p \rangle = 0$ and $\langle \tilde{v}_p(\vec{r}, t) \tilde{v}_p(\vec{r}', t') \rangle = 2k_B T \nabla^2 \delta(\vec{r} - \vec{r}') \delta(t - t')$ See Ref. [11] for further details of numerical implementation.

Simulations of the nucleation and growth of elastically misfitting 1T' domains that are coherently bound to a parent 1H crystal were performed as follows. Each simulation begins with a single crystal monolayer of 1H phase. A central triangular region with side length $960\Delta x$ is designated as the as-grown 1H island by setting $P(\vec{r}) = 0.01$ within the triangle (this maintains $\eta_p = 0$ inside the triangle throughout the simulation). Elsewhere $P(\vec{r})$ is set to zero, allowing 1T' domains to nucleate and grow beyond the initial triangular 1H phase island.

Input parameters employed for MoS₂/MoTe₂ were $\epsilon_{xx}^0 = 0.0058$, $\epsilon_{yy}^0 = 0.0584$, $\mu = 100$ GPa, $\nu = 0.24$, and $h = 0.35$ nm. Parameters common to all simulations were $\beta_p = 0.01225$, $a = 0.0007$, $b = 0.0042825$, $c = 0.0021$, $d = 1/30$, $M_p = 1$, $k_B T = 0.00001$, a discrete grid spacing $\Delta x = 1$, and a system size of $2000\Delta x \times 1600\Delta x$. Simulations employing Eq. (7) used a time step $\Delta t = 15$ while those employing Eq. (8) used $\Delta t = 5$.

Nucleation and growth of the 1T' phase occurs as follows. In simulations employing Eq. (7), linear gradients in a and b , from $(a,b) = (0.0007, 0.0042825)$ in the bulk to $(a,b) = (-0.0003, 0.0032825)$ at the triangle edge, were imposed within a $150\Delta x$ wide region outside the 1H triangle. This increases the driving force for 1T' formation directly at the edges, ensuring initial nucleation and outward growth of 1T' domains from the triangle edges.

Simulations employing Eq. (8) involved no such gradients in a and b , but were instead supplied with a steady, homogeneous flux of each 1T' variant, representing free Te and Mo. The η_p flux was introduced along the 1H triangle edges during the initial growth phase at a rate of $-1 \times 10^{-5}/\Delta t/(\Delta x)^2$. Once 1T' domains completely covered the 1H triangle edges, the source region was expanded with the growing 1T' domain fronts. This setup describes a steady flux of source material attaching to the 1H triangle edges and/or the top of the monolayer and diffusing toward the edges of the 1T' domains to drive growth.

Representative 1T' morphologies from growth simulations under various conditions are shown in Figure S6. In a-c, the misfit strain corresponding to Te compositions $x_i^{1H} = 0.75$ and $x_i^{1T'} = 0.94$ on the 1H and 1T' sides of the interface, respectively, was used, as inferred from the TEM-derived lattice parameters. The configuration shown in the main text is reproduced in Figure S6a for convenience of comparison. This simulation employed Eq. (7) dynamics and constant β_p . The resulting morphology demonstrates that elastic misfit between the 1H and 1T' phase alone can induce a needle-like 1T'

growth mode in the present experimental system. Anisotropy in $1T'$ edge energies also leads to elongated rectangle-like domains (see Figure S3 and S4), but the specific $1T'$ orientations observed in the experiments along each edge of the triangle and the enhanced elongation relative to isolated $1T'$ islands can be attributed to this elastic misfit effect.

Figure S6b further supports this conclusion by showing that only a modest accentuation of the average needle length to width ratio is observed when a 2-fold anisotropic $1T'$ interfacial energy similar to that computed from first-principles is included. Conditions are otherwise identical to those in Figure S6a. The degree of anisotropy employed corresponds to the lower bound estimated from the DFT results in Figure S3. A larger anisotropy would presumably further accentuate the needle morphologies, but we are unable to reliably simulate growth kinetics at the estimated degree of edge energy anisotropy due to issues with numerical implementation. The faceted interfaces that appear with large anisotropy tend to alter growth kinetics in unphysical ways, prohibiting direct comparison with results at small anisotropy.

Figure S6e simply confirms the necessary absence of $1T'$ needles when both misfit strain between $1H$ and $1T'$ phases and interfacial anisotropy are absent. Figure S6f further shows that anisotropy of the degree corresponding to the lower bound estimated from the DFT results in Figure S3 leads to edge orientation-dependent variant selection as in a-c, but that rounded wedge-shaped $1T'$ protrusions rather than distinctly oriented needle-shaped protrusions are obtained when elastic misfit is absent. Conditions in e and f are otherwise identical to those in a. Again, the tendency toward needle-like structures should increase with the degree of anisotropy.

Under different growth conditions either Eq. (7) or Eq. (8) may be the more appropriate description of the experimental system. However, comparison of the results from both approaches (compare Figure S6a and c) shows that both lead to qualitatively similar $1T'$ growth morphologies, albeit

with somewhat different needle lengths and widths. Hence, the morphologies observed in these simulations and the experiments are dominated by elastic misfit energies and edge energy anisotropies rather than kinetic details.

Comparison of Figure S6a and d shows that the nature of the elastic misfit between the 1H and 1T' phases can also qualitatively affect the growth morphology. Conditions in d are as in a except a shear-dominant misfit strain (i.e., $|R| = |(\epsilon_{xx}^0 + \epsilon_{yy}^0)/(\epsilon_{xx}^0 - \epsilon_{yy}^0)| \approx 0.5$) corresponding to Te compositions $x = 0$ and 1 on the 1H and 1T' sides of the interface, respectively, is employed. A relatively compact growth morphology is observed whenever the misfit strain is shear-dominant rather than dilatation-dominant ($|R| \geq 0.5$). A crossover from needle-like to compact 1T' structures occurs here for $x_i^{1H} \leq 0.11$ if $x_i^{1T'} = 1$.

These results together demonstrate that dilatation-dominant elastic misfit alone can induce needle-like growth morphologies in the absence of anisotropic 1T' edge energies and growth rates. Sufficiently large anisotropy also leads to needle-like structures. At the estimated misfit strains and computed anisotropy levels in the present systems, both effects are expected to drive the needle-like growth morphologies seen in our experiments (see the main text).

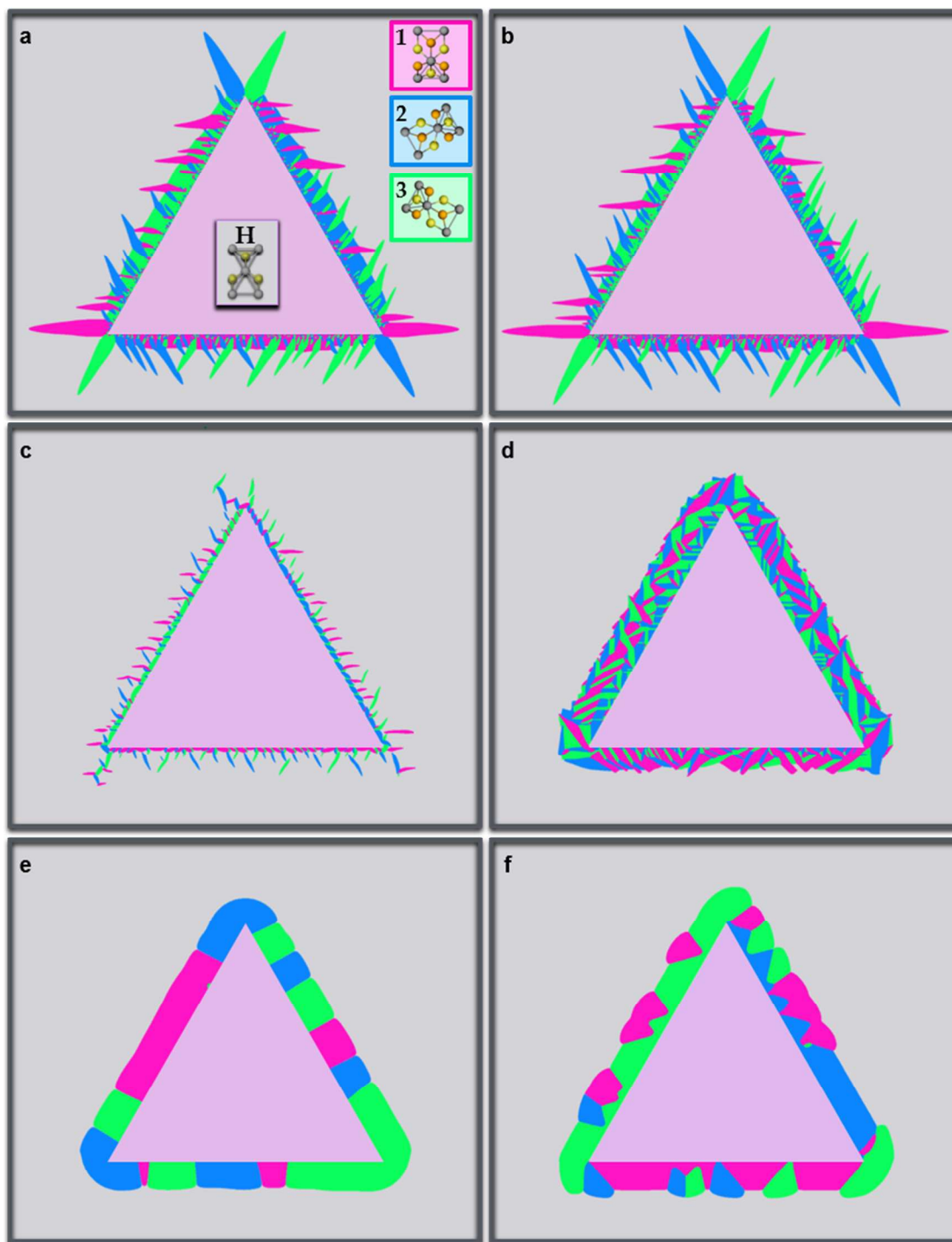


Figure S6. Simulated 1T' growth/transformation morphologies under various growth conditions designed to determine which factors dominate the experimentally observed island structures. In a-c the misfit (transformation) strain corresponding to $x_i^{1H} = 0.75$ and $x_i^{1T'} = 0.94$ on the 1H and 1T' sides of

the interface, respectively ($\epsilon_{xx}^0 = 0.58\%$, $\epsilon_{yy}^0 = 5.84\%$), is used. **a.** Equation (7) and constant $\beta_p(\phi) = 0.01225$ (as shown in the main text). The color scheme employed for 1T' domains is shown on the right. **b-f.** As **a** but with: **b.** 2-fold anisotropic interfacial energies $\beta_p(\phi) = 0.01225[1 + 0.149\cos(2\phi + \theta_p)]$, **c.** Dynamics given by Eq. (8), **d.** Shear-dominant misfit $\epsilon_{xx}^0 = -2.99\%$ and $\epsilon_{yy}^0 = 3.74\%$, corresponding to $x_i^{1H} = 0$ and $x_i^{1T'} = 1$ on the 1H and 1T' sides of the interface, respectively. **e.** Zero misfit $\epsilon_{xx}^0 = \epsilon_{yy}^0 = 0$. **f.** Zero misfit $\epsilon_{xx}^0 = \epsilon_{yy}^0 = 0$ and 2-fold anisotropic interfacial energies $\beta_p(\phi) = 0.01225[1 + 0.149\cos(2\phi + \theta_p)]$.

References

- [1] Shenoy, V. B.; Reddy, C. D.; Ramasubramaniam, A. & Zhang, Y. W. Edge-Stress-Induced Warping of Graphene Sheets and Nanoribbons. *Phys. Rev. Lett.* **2008**, 101, 245501.
- [2] Kresse, G. and Furthmüller, J. Efficiency of *ab-initio* Total Energy Calculations for Metals and Semiconductors Using a Plane-Wave Basis Set. *Comput. Mater. Sci.* **1996**, 6, 15.
- [3] Kresse, G & Furthmüller, J. Efficient Iterative Schemes for *ab initio* Total-Energy Calculations Using a Plane-Wave Basis Set. *Phys. Rev. B* **1996**, 54, 11169.
- [4] Blöchl, P. E. Projector Augmented-Wave Method. *Phys. Rev. B* **1994**, 50, 17953.
- [5] Perdew, J. P.; Chevary, J.; Vosko, S.; Jackson, K. A.; Pederson, M. R.; Singh, D. & Fiolhais, C. Atoms, Molecules, Solids, and Surfaces: Applications of the Generalized Gradient Approximation for Exchange and Correlation. *Phys. Rev. B* **1992**, 46, 6671.

- [6] Perdew, J. P.; Burke, K. & Ernzerhof, M. Generalized Gradient Approximation Made Simple. *Phys. Rev. Lett.* **1996**, *77*, 3865.
- [7] Zhou, S.; Han, J.; Sun, J. & Srolovitz, D. J. MoS₂ Edges and Heterophase Interfaces: Energy, Structure and Phase Engineering. *2D Mater.* **2017**, *4*, 025080.
- [8] Naylor, C. H.; Parkin, W. M.; Ping, J.; Gao, Z.; Zhou, Y. R.; Kim, Y.; Streller, F.; Carpick, R. W.; Rappe, A. M.; Drndic, M.; Kikkawa, J. M. & Johnson, A. T. C. Monolayer Single-Crystal 1T'-MoTe₂ Grown by Chemical Vapor Deposition Exhibits Weak Antilocalization Effect. *Nano Lett.* **2016**, *16*, 4297.
- [9] Chen, S.-Y.; Naylor, C. H.; Goldstein, T.; Johnson, A. C. & Yan, J. Intrinsic Phonon Bands in High-Quality. *ACS Nano* **2017**, *11*, 814.
- [10] Han, G. H.; Keum, D. H.; Zhao, J.; Shin, B. G.; Song, S.; Bae, J. J.; Lee, J.; Kim, J. H.; Kim, H.; Moon, B. H. & Lee, Y. H. Absorption Dichroism of Monolayer 1T'-MoTe₂ in Visible Range. *2D Mater.* **2016**, *3*, 1–6.
- [11] Berry, J.; Zhou, S.; Han, J.; Srolovitz, D. J. & Haataja, M. P. Dynamic Phase Engineering of Bendable Transition Metal Dichalcogenide Monolayers. *Nano Lett.* **2017**, *17*, 2473.
- [12] Wen, Y.; Wang, Y.; Chen, L.-Q. Effect of Elastic Interaction on the Formation of a Complex Multi-Domain Microstructural Pattern During a Coherent Hexagonal to Orthorhombic Transformation. *Acta Mater.* **1999**, *47*, 4375– 4386.
- [13] Wen, Y.; Wang, Y.; Chen, L.-Q. Phase-Field Simulation of Domain Structure Evolution During a Coherent Hexagonal-to-Orthorhombic Transformation. *Philos. Mag. A* **2000**, *80*, 1967–1982.
- [14] Wen, Y.; Wang, Y.; Chen, L.-Q. Influence of an Applied Strain Field on Microstructural Evolution During $\alpha_2 \rightarrow O$ - Phase Transformation in Ti–Al–Nb System. *Acta Mater.* **2001**, *49*, 13–20.